JGR Planets

RESEARCH ARTICLE

10.1029/2020JE006745

Key Points:

- We performed reverse impact experiments and shock-and-release experiments to probe the density and temperature of the liquid-vapor phase boundary
- The experimentally determined liquid-vapor dome does not agree with commonly used equation of state models
- Supercritical post-impact states are easier to achieve than previously modeled

Supporting Information:

Supporting Information may be found in the online version of this article.

Correspondence to:

E. J. Davies,
davies23@llnl.gov

Citation:

Davies, E. J., Duncan, M. S., Root, S., Kraus, R. G., Spaulding, D. K., Jacobsen, S. B., & Stewart, S. T. (2021). Temperature and density on the forsterite liquid-vapor phase boundary. *Journal of Geophysical Research: Planets*, *126*, e2020JE006745. https://doi.org/10.1029/2020JE006745

Received 28 OCT 2020
Accepted 6 FEB 2021

Temperature and Density on the Forsterite Liquid-Vapor Phase Boundary

E. J. Davies[1,2], M. S. Duncan[3], S. Root[4], R. G. Kraus[1], D. K. Spaulding[2], S. B. Jacobsen[5], and S. T. Stewart[2]

[1]Lawrence Livermore National Laboratory, Livermore, CA, USA, [2]Department of Earth and Planetary Sciences, U. California, Davis, CA, USA, [3]Department of Geosciences, Virginia Tech, Blacksburg, VA, USA, [4]Sandia National Laboratories, Albuquerque, NM, USA, [5]Department of Earth and Planetary Science, Harvard University, MA, USA

Abstract The physical processes during planet formation span a large range of pressures and temperatures. Giant impacts, such as the one that formed the Moon, achieve peak pressures of 100s of GPa. The peak shock states generate sufficient entropy such that subsequent decompression to low pressures intersects the liquid-vapor phase boundary. The entire shock-and-release thermodynamic path must be calculated accurately in order to predict the post-impact structures of planetary bodies. Forsterite (Mg_2SiO_4) is a commonly used mineral to represent the mantles of differentiated bodies in hydrocode models of planetary collisions. Here, we performed shock experiments on the Sandia Z Machine to obtain the density and temperature of the liquid branch of the liquid-vapor phase boundary of forsterite. This work is combined with previous work constraining pressure, density, temperature, and entropy of the forsterite principal Hugoniot. We find that the vapor curves in previous forsterite equation of state models used in giant impacts vary substantially from our experimental results, and we compare our results to a recently updated equation of state. We have also found that due to under-predicted entropy production on the principal Hugoniot and elevated temperatures of the liquid vapor phase boundary of these past models, past impact studies may have underestimated vapor production. Furthermore, our results provide experimental support to the idea that giant impacts can transform much of the mantles of rocky planets into supercritical fluids.

Plain Language Summary Collisions onto planets during planet formation can reach extreme pressures and temperatures. Giant impacts, like one that may have made the moon, reach pressures of millions of atmospheres. Decompression from such high pressures causes the material that makes up planets to melt and vaporize. To help predict the post collision structure of planets, we performed laboratory experiments on the mineral forsterite (Mg_2SiO_4) that recreates the extreme conditions of these collisions. We used the Z Machine, a facility at Sandia National Laboratories that can launch projectiles up to 40 km s^{-1} (almost 90,000 miles per hour), to measure the properties of forsterite once it has decompressed. We find that previous models of forsterite melting and vaporization do not match the experimental results found here. The results provide experimental support that giant impacts yield planets that may have mantles that are partially supercritical fluids, that behave like liquids and gases.

1. Introduction

During terrestrial planet formation, impacts were a widespread and fundamental process (Chambers, 2010), the scale of which ranged from small impacts between planetesimals to giant impacts such as the Moon-forming impact. The post-impact structures of a giant impact depend upon the specific parameters of the impact. The equations of state (EOS) of the constituent materials are necessary to enable calculation of the energy deposited by the event and the internal structure, including the amount of melting and vaporization. Previous work has found that energetic, high-angular momentum impacts create synestias (Lock & Stewart, 2017; Lock et al., 2018) and less energetic impacts form a more traditional planet and disk structures (Canup et al., 2013). Understanding the evolution of planetary bodies after a giant impact requires robust EOS models.

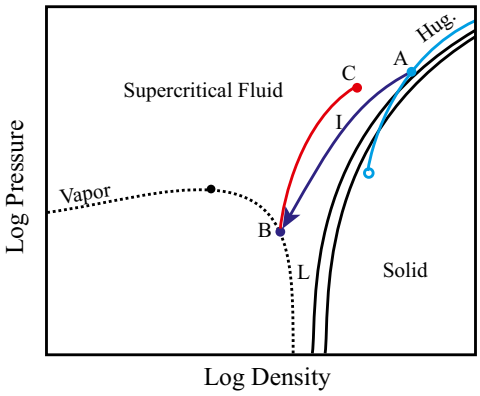

Figure 1. Schematic single-component phase diagram of the shock, release, and re-shock experiments to determine the temperature and density on the liquid-vapor phase boundary. In blue is the principal Hugoniot, the dark blue arrow is the isentropic release path, and in red is the re-shock Hugoniot from state B. The dotted black line is the unknown vapor curve with the critical point at the black dot. The solid black lines are the melt curve.

Giant impacts between Earth-sized planets can generate pressures and temperatures in excess of 500 GPa and 15,000 K. Subsequent decompression melts and vaporizes significant fractions of the constituent materials. Recent work has shown that vaporizing collisions are relatively common during planet formation in that almost all impacts onto large embryos create vapor (Davies et al., 2020; Kraus et al., 2012, 2015; Stewart & Ahrens, 2005). Wide-ranging EOS models are required that span the extreme conditions achieved during giant impacts as well as the subsequent decompression to the liquid-vapor phase boundary.

Hydrocode simulations of planetary collisions often use forsterite (Mg_2SiO_4), the Mg end-member of the olivine system, as a proxy for the bulk silicate composition of differentiated bodies. The most commonly used EOS for forsterite, M-ANEOS, is an extension of the Analytic Equations of State (ANEOS) code package (Thompson, 1990; Thompson & Lauson, 1974) which includes molecular vapor species. ANEOS was originally developed for silica in Melosh (2007). ANEOS-based material models require many input parameters that must be constrained by thermodynamic data.

The ANEOS models for forsterite used in previous giant impact studies were developed without experimental constraints for the vapor curve at high pressures and without measurements of the shock response above about 200 GPa. Recently, the shock states for forsterite were measured at pressures from 200 to 950 GPa, to determine the relationships between pressure (P), density (ρ), temperature (T), and specific entropy (S) (Davies et al., 2020; Root et al., 2018). Stewart et al. (2020) found substantial differences between previous ANEOS models for forsterite and these new data, and developed improvements to the ANEOS code package to improve the fit to experimental temperatures and entropies.

The liquid-vapor phase boundary is difficult to access experimentally for silicates because they have critical point temperatures that preclude static measurements. Evaporation experiments have determined the triple point for forsterite at 2,163 K and 5.2 Pa (Nagahara et al., 1994), but these experiments do not extend to the critical point. Previous studies determined the thermodynamic states on the liquid-vapor phase boundary of silica (Kraus et al., 2012) and iron (Kraus et al., 2015) and developed a technique to enable measurements of state variables with a dynamic shock-and-release experiment. In this work, we utilize this technique to provide the first experimental constraints on the forsterite liquid-vapor curve near the critical point.

In a planar shock experiment, a flyer plate generates a shock wave that propagates through the sample and compresses it uniaxially. The shock wave is a near discontinuous feature that separates ambient P, ρ, and energy states from high P, high ρ, and high energy shocked states. These shock states obey the one-dimensional Rankine-Hugoniot jump conditions derived from conservation of mass, momentum, and energy:

$$\frac{\rho}{\rho_0} = \frac{u_s}{u_s - u_p}, \tag{1}$$

$$P - P_0 = \rho_0 u_s u_p, \tag{2}$$

$$E - E_0 = \frac{1}{2}(P + P_0)\left(\frac{1}{\rho_0} - \frac{1}{\rho}\right), \tag{3}$$

where the subscript naught indicates the initial condition, u_s is the shock wave velocity, u_p is the particle velocity, V is specific volume, and E is the specific internal energy. The collection of all possible shock states for a single initial condition is a curve known as the Hugoniot. The Hugoniot with initial conditions at standard temperature and pressure conditions (STP) is the principal Hugoniot. An illustration summarizing the thermodynamic paths utilized in our experiments is given in Figure 1. The principal Hugoniot, with example shock state at point A, is shown by the blue line in Figure 1.

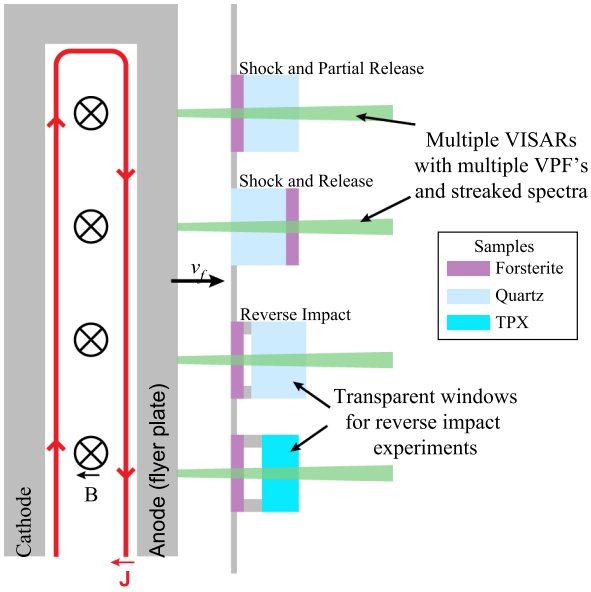

Figure 2. Generalized schematic of the flyer plate experiments on the Sandia Z Machine. In each experiment, both the anode and cathode are 1.2 mm thick aluminum flyer plates that impact target panels with several science samples and diagnostic windows. The ability to field up to 14 samples per shot enables multiple types of measurements in a single experiment: Shock and partial release, shock-and-release, and reverse impact experiments.

Table 1
Summary of Variables Used in This Work

Symbol	Description	Units
u_s	Shock velocity	km/s
u_p	Particle velocity	km/s
T	Temperature	K
P	Pressure	Pa
S	Specific entropy	J/K/kg
E	Specific internal energy	J/kg
V	Specific volume	m^3/kg
ρ	Density	kg/m^3
v_i	Impact velocity	km/s
v_f	Liquid flyer velocity	km/s
c_s	Bulk sound speed	km/s
C_0	Intercept for a linear $u_s - u_p$ Hugoniot	km/s
s	Slope for a linear $u_s - u_p$ Hugoniot	-
R	Shock front reflectivity	-
Z	Shock impedance	$kg/m^2/s$
γ	Grüneisen parameter	-
α	Absorption coefficient	m^{-1}
L_{mfp}	Mean free path	m

The decompression path from a shock state provides an opportunity to probe the temperature and density of the liquid-vapor phase boundary. Once the shock wave reaches a free surface, a rarefaction wave propagates back into the shocked sample, decompressing the sample. The rarefaction wave is a pressure wave that propagates at the speed of sound and is assumed to be isentropic in a liquid (dark blue decompression path in Figure 1). The rarefaction also accelerates the decompressing material, where the acceleration depends upon the sound speed. During decompression from a sufficiently strong shock, the isentrope will intersect with the liquid-vapor phase boundary, for example, at point B in Figure 1. To continue decompressing, the sample must begin to vaporize. The phase change also represents a discontinuity in the sound speed, leading to separation of decompression waves above and below the liquid-vapor phase boundary. Material is therefore inertially trapped between the two waves at the density of the liquid-vapor phase boundary. The thermal emission from this liquid layer can also be measured to constrain the temperature of this state (B) on the phase boundary.

The density of the liquid layer at state B in Figure 1 is determined by conducting a reverse impact experiment, where the accelerated liquid flyer plate is the material of interest. In a reverse impact experiment, such as Kraus et al. (2012) and Kraus et al. (2015), a standard window is placed downrange of the sample by a known gap distance. The liquid layer traverses this gap and impacts the window, generating a shock in the trapped material and in the window. The shock that propagates back into the liquid flyer lies on the Hugoniot with initial conditions on the liquid branch of the liquid-vapor phase boundary (e.g., shock state C on the reshock Hugoniot shown as the red line in Figure 1).

In this work, we present data obtained through the Z Fundamental Science Program at Sandia National Laboratory's Z Machine. Our experiments exploit the shock-and-release thermodynamic path to attain temperatures and densities on the liquid branch of the liquid-vapor phase boundary.

2. Experimental Methods

Shock compression experiments were performed at the Sandia Z machine using a magnetic drive generated by an intense current pulse. The large current and field densities generate magnetic pressures up to 650 GPa that can accelerate aluminum flyer plates up to 40 km/s (Lemke et al., 2005). Figure 2 shows a schematic of the experimental configuration. The principal diagnostic in this work was the Velocity Interferometer System for Any Reflector (VISAR) (Barker & Hollenbach, 1972; Barker & Schuler, 1974), which measures flyer plate velocity, shock wave velocity, and transit times. Selected samples also employed a Streaked Visible Spectrometer (SVS) to measure the emission spectrum from the sample, as used in previous experiments (Root et al., 2018). All variables in this work are defined in Table 1, and Hugoniot relations are defined in Table 2.

Two types of experiments were performed for this work that take advantage of the shock-and-release thermodynamic path described in Section 1. The first type of experiment was a reverse impact experiment, where forsterite was shocked and then decompressed across a vacuum gap of

Table 2
Equations for the Principal Hugoniots of Materials Used in This Work

Material	Hugoniot equations	Reference
Forsterite	$u_s(u_p) = 4.632 + 1.455u_p + (4.291E-03)u_p^2 - (7.844E-04)u_p^3$	(1)
	$T(u_s) = -183.188u_s + 15.605u_s^2 + 2.785u_s^3$	(1)
	$S(P) = -28691P^{-0.5} + 152.8P^{0.5} - 0.0208P^{1.5} + 3{,}680$	(2)
	$\gamma(\rho) = \gamma_\infty + (0.377 - \gamma_\infty)\left(\frac{\rho_0}{\rho}\right)^{3.705} + 0.657e^{-(\rho-4930)^2/1192^2}$	(2)
α-quartz	$u_s(u_p) = 1.754 + 1.862u_p - (3.364E-02)u_p^2 + (5.666E-04)u_p^3$	(3)
TPX	$u_s(u_p) = 1.795(\pm.018) + 1.357(\pm.003)u_p - 0.694(\pm.027)u_p e^{-0.273(\pm.011)u_p}$	(4)

Notes. Errors on the parameters for us(up) for TPX are given. Uncertainty for $\gamma(\rho)$ of forsterite is 32%. Uncertainty for the others have co-variance matrices included in the supplemental materials in Table D1. The forsterite principal Hugoniot equations have a range of validity from 200 to 950 GPa, and the initial density (ρ_0) is 3,220 kg/m^3. The forsterite $\gamma(\rho)$ function is valid from 2,597 to 6,500 kg/m^3, where $\gamma_\infty = 2/3$ and $\rho_0 = 2{,}597(\pm 11)$ kg/m3. The quartz principal Hugoniot us(up) equation have a range of validity 40–800 GPa, and the initial density is 2,651 kg/m3. TPX principal Hugoniot equations have a range of validity up to 985 GPa, and the initial density is 833 kg/m^3. The material-specific us(up) equations can be transformed to pressure, specific volume and specific internal energy via the Rankine-Hugoniot conservation equations. References: (1) Root et al. (2018), (2) Davies et al. (2020), (3) Knudson and Desjarlais (2013), (4) Root et al. (2015).

known distance. Reverse impact experiments (following shock-and-release) were previously conducted in Kraus et al. (2015) to measure the density of liquid iron on the vapor curve. The theoretical development of the shock-and-release technique to effectively generate a "liquid flyer plate" was presented in Kraus et al. (2012). We used synthetic single-crystal forsterite samples from MolTech GMBH and Princeton Scientific Corp. The forsterite was oriented on the [001] axis, which has an index of refraction of $\bar{n}_{001} = 1.651$. The samples had an initial density of $\rho_0 = 3.22 \pm 0.01$ g/cm^3 (Deer et al., 2013).

When the shock reaches the down range free surface of the sample, we measured the time of flight of the uniaxially expanding forsterite across gaps of known thickness to determine the velocity of the liquid flyer plate. The decompressing forsterite then strikes a standard window, and we determined the shock state generated in the window by measuring the shock velocity using VISAR and applying the known material Hugoniot. Multiple gap distances on the same experiment allowed us to constrain the velocity of the uniaxially expanding forsterite, and multiple windows of different impedance (initial density) helped us constrain the density of the liquid layer using standard impedance matching techniques (Sections 2.1 and 3.1).

The second type of experiment was a shock-and-release experiment with a quartz window backed by a forsterite sample. The quartz shock temperatures were calibrated by Hicks et al. (2006); Millot et al. (2015) with reflectivity corrections from Celliers et al. (2010) and were used as a standard reference material to determine the relative luminosity of the unknown mineral sample. Quartz shock velocities were used to calculate the shock temperature by interpolating between existing data and propagating the uncertainties of the calibrated reference and measured shock velocity. The emission spectra of the shocked and released forsterite were measured using the SVS diagnostic. The post-shock emission measurements are described in detail in Section 2.2. Reverse impact and shock-and-release experiments were not performed together because the SVS was commissioned concurrent with this project.

2.1. Reverse Impact Experiments

This section describes the reverse impact experiments in detail, providing new illustrations of the main features observed in the raw data and their interpretations. The VISAR system was the primary diagnostic, measuring the velocities of reflecting surfaces and reflecting shock fronts. Additionally and most importantly, VISAR captured time of flight transit measurements using changes in the reflected intensity of light

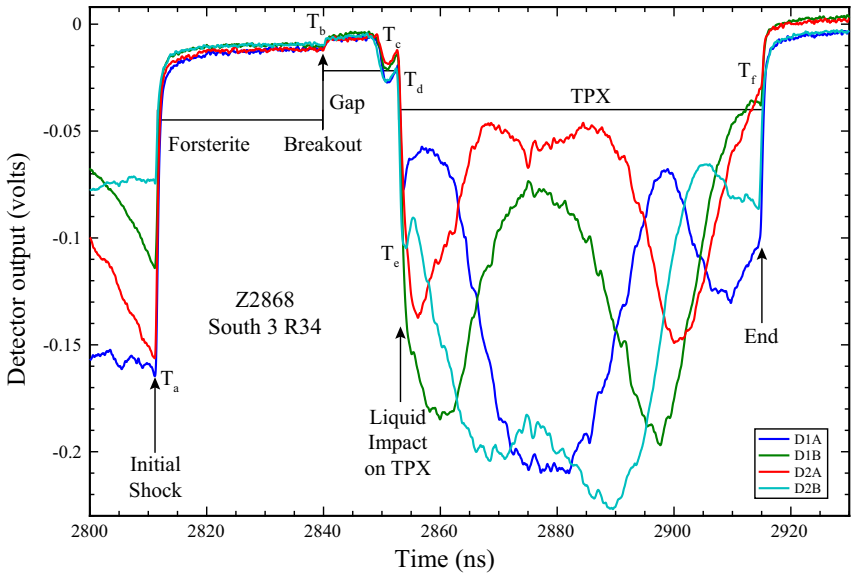

Figure 3. Example of raw VISAR data, showing intensity of light with time where the principal source of light is the VISAR laser at 532 nm. A schematic of the main events observed in the data is presented in Figure 4. For this detector, higher intensities of light produce a more negative voltage signal. See text for discussion of the main events. VISAR, Velocity Interferometer System for Any Reflector.

on the detector. In these reverse impact experiments, the forsterite samples were only weakly reflecting at the pressures achieved and material traveling within the gap was not measurably reflecting. Time of flight measurements were used when reflecting surfaces could not be measured. An example of raw VISAR data are shown is Figure 3.

Initially, the highly reflective aluminum flyer has a strong signal (large negative value) given its high reflectivity. Upon impact with the forsterite (at time T_a), the signal approaches a small value because the forsterite shock front is only weakly reflecting at the pressures achieved (Root et al., 2018). The signal further approaches zero upon free-surface breakout (T_b). The voltage drop in the gap represents the vapor stagnating against the TPX window, where the slight decrease in light directly after the increase is a weak shock in the TPX window (T_c). The sudden increase in light at time T_d is caused the liquid flyer striking the window and generating a strong shock. The increase in contrast of the VISAR (resolved phase shifted signals) is caused by the strong reflecting shock in the window overtaking the weak shock (T_e). The final drop to zero signal is the shock reaching the free surface of the window (T_f).

In a reverse impact experiment, the sample is initially impacted by the flyer and shocked to a state on the principal Hugoniot (at time T_a). VISAR is used to measure the shock wave velocity directly when the shock is strongly reflecting. If the shock front is weakly reflecting, the shock wave velocity is determined by the transit time through the known sample thickness. The shock Hugoniots for forsterite (Root et al., 2018) and the standard windows: α-quartz (Knudson & Desjarlais, 2009, 2013) and TPX (Root et al., 2015), are well-characterized, such that measuring u_s provides P and ρ of the shock state via the Rankine-Hugoniot relations.

When the shock front reaches the downrange free surface (at time T_b), it decompresses by a rarefaction wave, which propagates up range back into the shocked sample. The decompression results in an acceleration for which the expansion velocity, $u_{p,exp}$ is given by the Riemann integral (Rice et al., 1958),

$$u_{p,exp} = u_{p,in} - \int_{P_{in}}^{P_{amb}} \frac{dP}{\sqrt{\left(-\partial P / \partial V\right)_S}} = u_{p,in} - \int_{P_{in}}^{P_{amb}} \frac{V}{c_s} dP, \quad (4)$$

where the subscript S in the derivative denotes an isentrope, $u_{p,in}$ is the initial particle velocity given by the Rankine-Hugoniot jump conditions, P_{in} is the pressure of the initial shock state, and P_{amb} is the

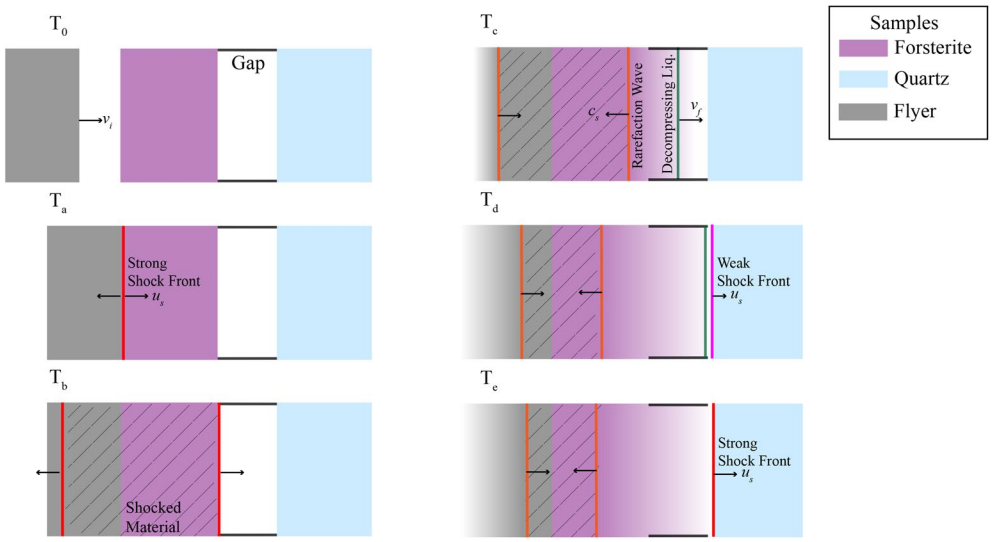

Figure 4. Cartoon of the main events in the reverse impact experiment observed in the raw data shown in Figure 3.

decompressed pressure. As the sample decompresses into the gap, the leading edge decompresses the fastest and accelerates more quickly than up range material. The unloading process requires a decrease in density to satisfy the isentropic decompression path, such that the decompression is limited in time by the expansion velocity. Thus, during decompression, the densities are the lowest at the leading edge of the expanding sample and increase in the up range direction.

Phase decomposition is an important effect to consider in the context of this work. Kraus et al. (2012) considered the time scales of fragmentation, nucleation and growth, and spinodal decomposition for silica decompressing via an isentrope near the critical point. Kraus et al. (2012) suggested that phase separation occurred by nucleation and growth at the phase boundary rather than spinodal decomposition because the timescale of spinodal decomposition is orders of magnitude longer than nucleation and growth. For a forsterite isentrope intersecting the liquid-vapor phase boundary near the critical point, phase separation likely occurs by the same mechanism. Thus, the results reported in this work are asserted to correspond to the liquid-vapor phase boundary, rather than the extended spinodal states. Furthermore, incongruent vaporization must be addressed as compositional separation between the liquid and vapor phases would complicate this work. Iron bearing olivine has been shown to vaporize incongruently in experiments performed by Costa et al. (2017). However, in the absence of iron, forsterite vaporizes congruently under equilibrium conditions, as shown in Nagahara et al. (1994). Thus, when the isentropic decompression path intersects the liquid-vapor phase boundary, forsterite is asserted to vaporize congruently.

Decompression upon shock breakout at the free surface is achieved by a rarefaction fan. Unlike a shock, rarefaction wave spreads out into a fan as it propagates because the sound speed decreases with decreasing pressure. At the liquid-vapor phase boundary, there is an abrupt and large change in the sound speed. As the material decompresses isentropically, the path crosses the liquid-vapor phase boundary. The discontinuity separates the rarefaction wave by splitting the decompression wave. The downrange section of the wave, within the liquid-vapor dome, accelerates more quickly than the up range section, which is still above the liquid-vapor dome. The velocity differential between the waves creates a portion of liquid that is inertially trapped at the liquid-vapor phase boundary at point B in Figure 5 at time (T_c). The rarefaction fan is calculated using the method of characteristics in Lagrangian coordinates (e.g., Kraus et al., 2012; Zel'Dovich & Raizer, 2002). Using the revised ANEOS forsterite model from Stewart et al. (2020), the 5,335 J/K/kg release isentrope from a 430 GPa shock is given in Figure 5 and the slope of the associated characteristics are given as

$$\left(\frac{dh}{dt}\right)_i = \frac{\rho_i c_{s,i}}{\rho_0}, \tag{5}$$

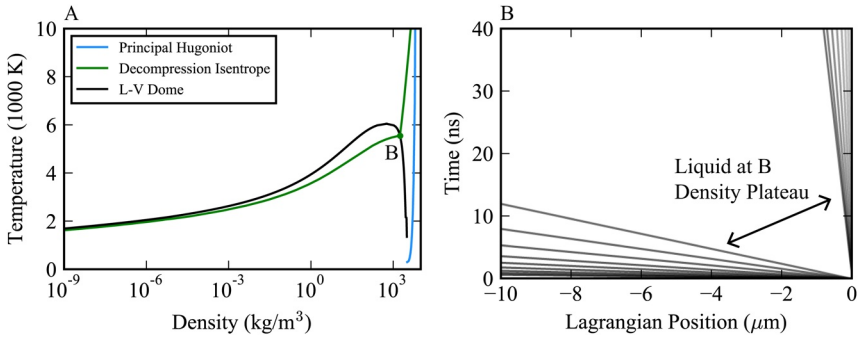

Figure 5. (a) Release isentrope in green from a 430 GPa shock, similar to the highest reverse impact experiment, in ρ-T space, starting from the principal Hugoniot (blue) and intersecting the liquid-vapor phase boundary (black) at point B (Figure 1). (b) Characteristics in Lagrangian coordinates, showing the plateau in the density profile that occurs at the intersection of the phase boundary. Higher density characteristics are opaque and opacity decreases with decreasing density.

where h is the Lagrangian coordinate and the subscript i denotes specific characteristic ρ and c_s. The characteristic curves, starting from the free surface at the Lagrangian position 0, define the propagation of the rarefaction wave up range into the sample (Figure 5). Each characteristic curve describes the propagation of disturbances from the free surface based on the density and sound speed, such that higher density and sound speed characteristics propagate faster than lower density and sound speed characteristics. The discontinuity in sound speed at the liquid-vapor phase boundary creates a plateau in density that thickens over time. We refer to the region of material trapped at state B as the liquid layer or "liquid flyer".

In the gap between the sample and window, the decompressing material expands until it impacts the down range window (at time T_d). The window is initially impacted by material, which is within the liquid-vapor dome, or the co-existence region of liquid and vapor. The liquid-vapor mixture stagnates against the standard window, causing a small intensity increase in signal return of the VISAR (Figure 3). As the liquid-vapor mixture builds up against the window, the signal intensity increases until the window becomes opaque, indicating a weak shock in the window. The magnitude of this change (if it occurs during the experiment) is entirely dependent upon window material and shock pressure in the forsterite sample. For example, shot Z2792, which had a forsterite shock pressure of ~330 GPa had reverse impact experiments with α-quartz and TPX windows. The α-quartz window is not shocked strongly enough by the vapor to become opaque, yet the TPX window does become opaque. Material at the liquid branch of the liquid-vapor phase boundary impacts shortly after, driving a strong shock in the window that quickly becomes reflecting when it overtakes the weak shock (T_e). Higher density liquid behind the inertially trapped material drives a ramp compression velocity profile at later times.

In a reverse impact experiment, three measurements are paramount. First, the shock state of the sample was measured by impedance matching from shock velocities that were determined by either a reflecting shock measurement or a shock transit time measurement through the sample. For this work, the shock transit time measurement uncertainty was large because the free surface breakout of the shock front was not always clear, although it was typically observable. Second, the liquid flyer velocity of the gap was measured, through a time of flight measurement. Third, the shock state in the window was determined through a direct shock velocity measurement determined by the reflecting shock velocity profile using the VISAR diagnostic and the known principal Hugoniot. Determining the shock state of the window driven by the inertially trapped liquid wall gives P and u_p in the liquid layer.

The velocity measurements are presented in Table 3. Interpretation of different events in the VISAR data is aided by hydrocode simulations of each experiment, which is discussed in section Appendix A of Supporting Information. These observed experiment parameters are used in Section 3.1 to calculate the density of the inertially trapped liquid layer.

Table 3
Experimental Measurements From the Reverse Impact Experiments on Forsterite: Impact Velocity of the Aluminum Flyer Plate (v_i), Shock Velocities (u_s) in the Sample and Window, and the Velocity of the Liquid Flyer Plate (v_f)

Shot #	Window material	v_i (km/s)	Sam. u_s (km/s)	Win. u_s (km/s)	Gap dist. (μm)	v_f (km/s)
Z2792 N1	TPX	14.68 ± 0.69	14.38 ± 0.13	15.72 ± 0.1	502 ± 10	15.30 ± 0.32
Z2792 N4	α-quartz	14.69 ± 0.03	14.50 ± 0.19	13.62 ± 0.05	497 ± 5	15.52 ± 0.25
Z2792 S3	TPX	14.69 ± 0.02	14.56 ± 0.20	15.84 ± 0.05	204 ± 4	15.45 ± 0.45
Z2792 S6	TPX	14.72 ± 0.03	14.79 ± 0.33	15.90 ± 0.15	800 ± 5	15.43 ± 0.19
Z2868 N1	TPX	15.82 ± 0.02	15.39 ± 0.14	16.40 ± 0.05	487 ± 6	16.38 ± 0.21
Z2868 N4	α-quartz	15.75 ± 0.01	15.50 ± 0.10	14.05 ± 0.05	489 ± 3	16.46 ± 0.25
Z2868 S3	TPX	15.64 ± 0.02	15.45 ± 0.15	16.60 ± 0.05	211 ± 9	16.50 ± 0.75
Z2868 S3	TPX	15.62 ± 0.01	15.34 ± 0.19	16.48 ± 0.02	794 ± 6	16.37 ± 0.21
Z2879 N1	TPX	12.83 ± 0.01	13.57 ± 0.30	13.98 ± 0.05	499 ± 16	12.96 ± 0.43
Z2879 N4	α-quartz	12.87 ± 0.03	13.35 ± 0.43	12.03 ± 0.02	495 ± 7	12.91 ± 0.23
Z2879 S2	α-quartz	13.81 ± 0.04	14.03 ± 0.16	12.71 ± 0.03	236 ± 40	14.66 ± 2.52
Z2879 S3	TPX	13.77 ± 0.03	14.02 ± 0.24	14.81 ± 0.03	212 ± 9	14.82 ± 0.67
Z2879 S5	α-quartz	13.78 ± 0.02	13.87 ± 0.22	12.81 ± 0.03	780 ± 6	14.07 ± 0.14
Z3422 S2	α-quartz	17.32 ± 0.01	16.34 ± 0.15	14.56 ± 0.05	506 ± 3	17.76 ± 0.15
Z3422 S3	α-quartz	17.34 ± 0.02	16.29 ± 0.15	14.55 ± 0.06	317 ± 7	17.86 ± 0.42
Z3422 S5	TPX	17.38 ± 0.03	16.27 ± 0.24	17.58 ± 0.17	506 ± 2	17.89 ± 0.19
Z3422 S6	TPX	17.39 ± 0.03	16.36 ± 0.15	17.38 ± 0.05	308 ± 2	17.97 ± 0.24

2.2. Post-Shock Thermal Emission

The purpose of this type of experiment is to measure the shock temperature and the temperature of the inertially trapped liquid layer that was described in Section 2.1. The temperature of this layer is the temperature of the liquid vapor phase boundary (point B in Figure 5). This experiment uses VISAR to measure the shock velocity in the sample to determine the shock state. When the shock is released into vacuum, for example, the second from top configuration shown in Figure 2, the thermal emission drops substantially with the onset of decompression. In addition, the thermal emission in the visible region of the electromagnetic spectrum is recorded using an SVS camera. The SVS camera system has previously been demonstrated for use in shock experiments in Root et al. (2018). The SVS diagnostic provides key constraints for temperature as it measures the emission spectrum with resolution in both time and wavelength. The principal method is to use a quartz-referenced calibration that is described in Root et al. (2018), which uses an α-quartz standard window as an in situ calibration source to measure the system response function. The α-quartz temperature and reflectivity response are taken from (Hicks et al., 2006; Millot et al., 2015) with reflectivity corrections from (Celliers et al., 2010).

An example of thermal emission data is shown in Figure 6. The aluminum flyer initially impacts the α-quartz standard, and the shock front in the quartz then propagates into the forsterite sample. As in the reverse experiment, VISAR is utilized to measure u_s. The $u_s - u_p$ relations for α-quartz and forsterite are well-characterized, such that the shock state is well-determined by a measurement of u_s. As in Section 2.1, when the shock front reaches the downrange free surface of the forsterite sample, it decompresses by a rarefaction wave. The result is the same inertially trapped liquid wall as previously described. A small amount of liquid-vapor mixture is decompressed ahead of the liquid layer. If the absorption from the liquid-vapor mixture is small, this liquid layer is the principal source of thermal emission after shock breakout at the free surface.

There are two major concerns in the analysis of the thermal emission from the liquid layer. First, the optical thickness of the inertially trapped liquid wall must be large enough to shield the up range material. Shock fronts for forsterite in the liquid region of the forsterite principal Hugoniot are typically weakly reflecting and opaque (Root et al., 2018). As the sample decompresses from the opaque or reflecting shock state,

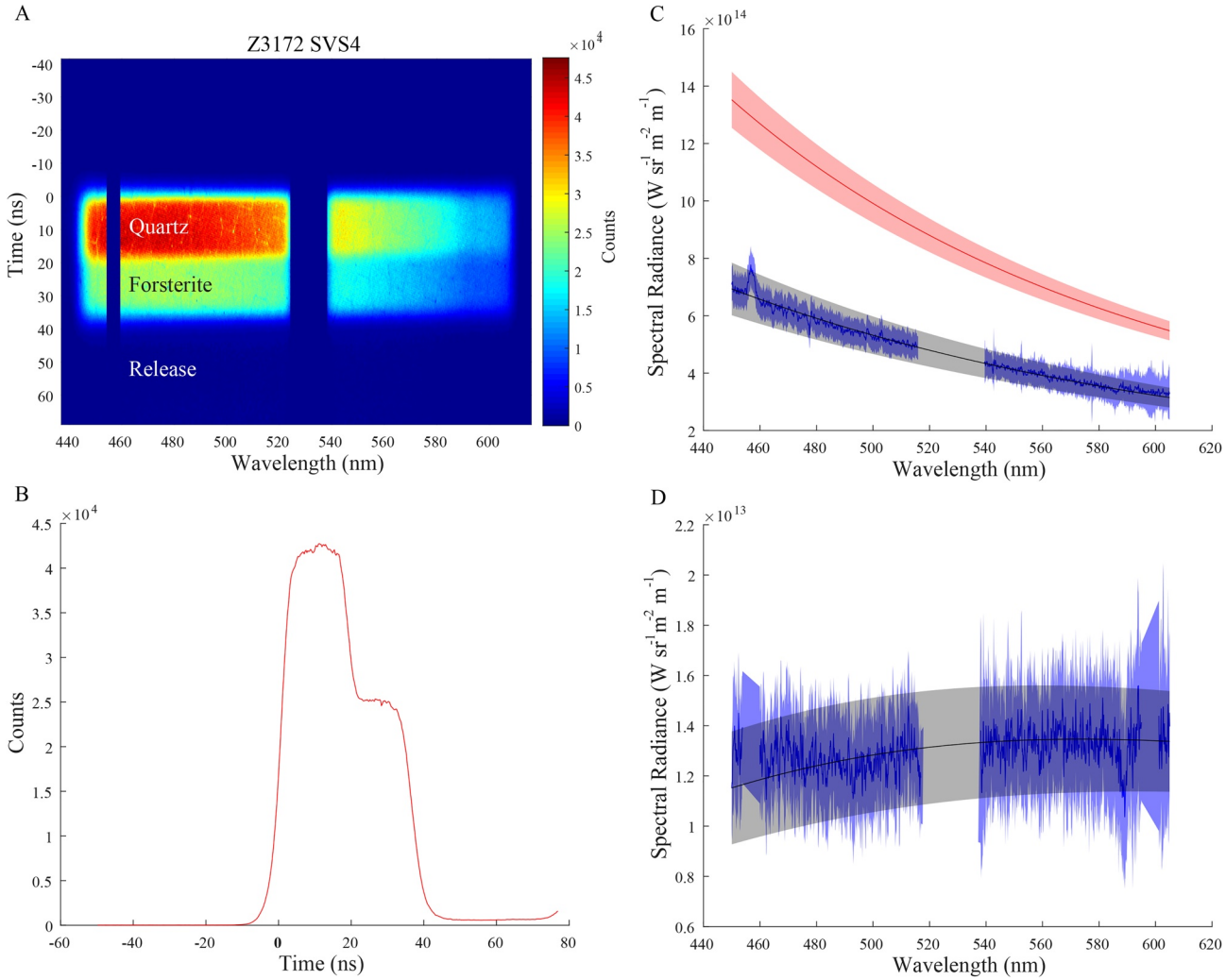

Figure 6. Thermal emission data from SVS4 from shot Z3172 N5 which had a shock pressure of 450.7 ± 4.9 GPa. (a) The SVS streak camera records thermal emission over time, resolved in wavelength. Events of the experiment are easily distinguished; pre-impact before time 0, quartz shock from 0–18 ns, forsterite shock from 20 to 35 ns, and post-shock emission from 40 to 70 ns. (b) Vertical line out over wavelengths 475–485 nm in time from (a). Post shock emission has on order of 100s of counts. (c) Ideal greybody for quartz (red line), horizontal lineout of forsterite data from 24 to 30 ns and (blue), and a fitted greybody (black line). (d) Horizontal lineout of post-shock emission from 50 to 60 ns, and its fitted blackbody (black line). For (c and d) uncertainty for data and fits are given by the associated envelopes. SVS, Streaked Visible Spectrometer.

the thickness of the inertially trapped liquid layer increases. If the optical depth of the liquid is similar to the thickness of the liquid layer, or transparent, then emission from the hotter and higher density region of the sample will contaminate the measurement. If this were the case, the measured emission spectrum would be a combination of the emission from the liquid layer and emission from higher density, up range material. Second, the decompressing liquid-vapor mixture that leads the liquid layer may absorb a non-negligible amount of photons. Release temperature experiments on silica combined with first principles molecular dynamics simulations noted that vapor thicknesses less than 200 μm have negligible absorption at visible wavelengths (Kraus et al., 2012). For Mg_2SiO_4, the vapor phase includes Mg and MgO (Townsend et al., 2020) complicating the absorption spectra of the liquid-vapor mixture. Absorption by the liquid-vapor mixture changes with time because of the creation of more vapor as the rarefaction waves propagate up range, thickening the mixed phase layer. Figure 6 shows that during the experiment, the steady shock in the forsterite and subsequent emission upon release are constant in intensity with time and are well fit by ideal greybodies, suggesting that in the visible spectrum, the inertially trapped liquid wall is optically thick and absorption by the vapor is not significant over the length scales of these experiments.

Table 4
Shock and Release Experiment Thermal Emission Results

Shot #	v_i (km/s)	P (GPa)	Sam. u_s (km/s)	S J/K/kg	Win. u_s (km/s)	Sam. T (K)	Sam. R (−)	Rel. T (K)
Z3033 N7	18.86 ± 0.06	496.8 ± 4.8	17.47 ± 0.21	5,571 ± 460	16.93 ± 0.39	16,104 ± 1,654	0.081 ± 0.026	5,063 ± 522
Z3172 N5	17.84 ± 0.05	450.7 ± 4.9	16.78 ± 0.20	5,372 ± 460	16.24 ± 0.06	13,758 ± 727	0.047 ± 0.022	5,051 ± 167
Z3172 S5	19.25 ± 0.04	517.3 ± 5.2	17.76 ± 0.23	5,650 ± 460	17.27 ± 0.04	16,770 ± 1,270	0.089 ± 0.022	5,174 ± 182

Notes. The shock states of these experiments were previously reported in Root et al. (2018). Specific Entropy for these shock states are calculated from the forsterite entropy relation in Table 2. Release temperatures are apparent temperatures without correction for leading liquid-vapor mixture.

Apparent shock and release temperatures from our experiments are given in Table 4. Notably these apparent temperatures are from liquid condensates suspended in the vapor cloud. These condensates affect the radiative transfer of emission from the liquid layer, which is discussed in detail in Kraus et al. (2012). This effect is not taken into account in the reported apparent T in Table 4: Instead a simple radiative transfer model is used to aid interpretation of the data in Section 3.2.

3. Results and Discussion

3.1. Liquid Flyer Density

From the reverse impact data, we calculated the density of the liquid forsterite before it impacts the standard window. However, certain material properties must first be known or determined to calculate this liquid density. In this section, we identify the required properties, determine their values, and use them to calculate the density of the liquid layer.

The Rankine-Hugoniot jump conditions relate the thermodynamic states on either side of a shock front, which must satisfy the conservation equations of mass, momentum, and energy. In a steady shock experiment, the shock state of a sample is determined by measuring the shock velocity in the shocked sample and using the impedance matching technique (Figure 7a) yielding P and ρ. The Hugoniot is the collection of possible end states of a shock starting from a single initial condition, but it is not a thermodynamic path itself. The straight line connecting the two states is the shock thermodynamic path and is called the Rayleigh line and is defined by Equation 2. The Rayleigh line has a slope that is defined by the initial density, ρ_0 and the measured u_s. In the reference frame of the experiment, the flyer's Hugoniot is reflected about the flyer velocity, and the intersection of the known flyer velocity and the sample's Rayleigh line is the shock state of the sample. This method relies on knowledge of the $u_s - u_p$ relationship of the flyer in the experiment,

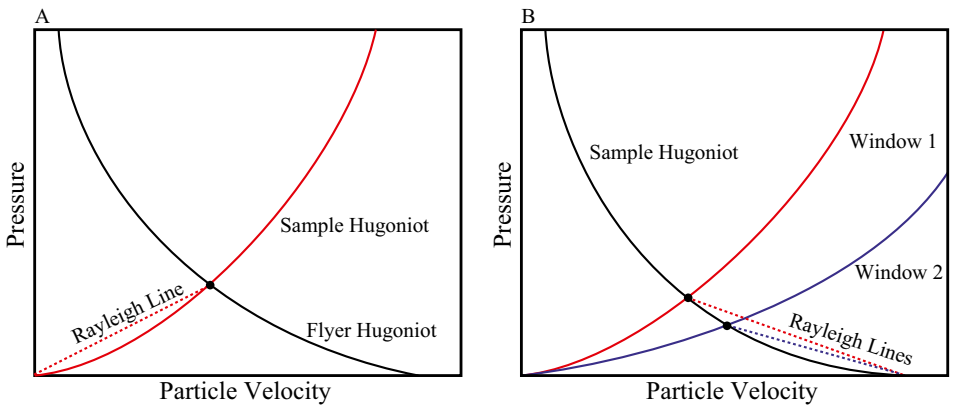

Figure 7. (a) Schematic of a typical steady shock experiment, where the red dashed line is the Rayleigh line, the red curve is the unknown sample Hugoniot, and the black curve is the known flyer Hugoniot. The intersection between the reflected flyer Hugoniot and the sample Rayleigh line is the shock state achieved by the experiment, which lies on the sample Hugoniot by definition. (b) Schematic of the reverse impact experiment, where shock states of the windows are determined by their known Hugoniots. Impedance matching the shock states in the windows with the unknown liquid flyer gives two P and u_p states to use to constrain the initial density of the liquid flyer.

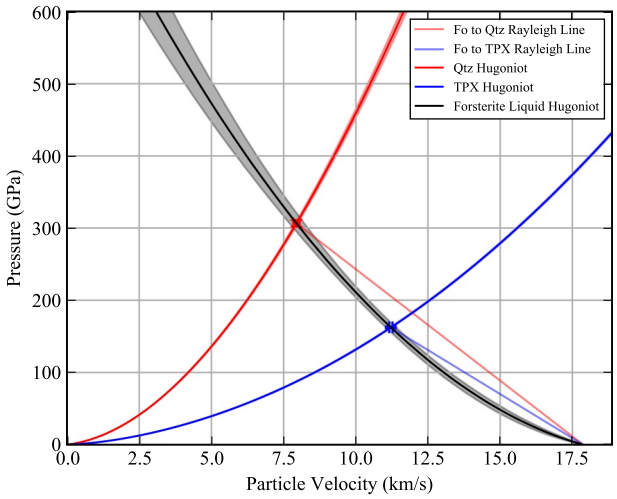

Figure 8. Shock states, window Hugoniots, liquid Rayleigh lines, and a fitted linear Hugoniot for shot Z3422 which generated a shock pressure of 428.53 ± 2.05 GPa in forsterite. Fitted values for C_0 and s are given in Table 5 along with the calculated density of the liquid forsterite flyer.

the flyer velocity, and the initial density of the flyer. In a typical shock experiment, these properties are measured before the experiment (initial densities), measured in the experiment (shock velocity and flyer velocity), or known beforehand, as in the case of the $u_s - u_p$ relationship of the standard flyer.

In a reverse impact, the flyer's Hugoniot is unknown and we used the standard impedance matching technique to determine the shock state of the liquid during impact with the down range window (Figure 7b). The Rayleigh line for the flyer in the laboratory reference frame is defined by

$$P - P_0 = \rho_0 u_s (v_f - u_p), \tag{6}$$

where v_f is the liquid flyer velocity. For the shock states considered in this work, P and u_p are given by the shock state of the window determined by impedance matching, P_0 is negligible, and v_f is measured (Table 3). The ρ_0 and u_s of the liquid flyer are both unknown. The shock impedance, Z, is defined here as the product of ρ_0 and u_s and is solved from Equation 6, and in the laboratory reference frame is

$$Z_i = \frac{P_i}{v_f - u_{pi}}, \tag{7}$$

where the subscript i denotes the material.

Returning to the Rayleigh lines, high pressure liquid Hugoniots, including liquid silicates have been empirically shown to be well represented by a linear Hugoniot in the mega-bar regime (e.g., Asimow, 2018). Assuming that the liquid flyer follows a linear Hugoniot ($u_s = C_0 + s u_p$), Equation 6 becomes

$$P = \rho_0 (C_0 + s(v_f - u_p))(v_f - u_p), \tag{8}$$

where C_0 is the sound speed in liquid, and s is the slope of the linear Hugoniot. For a given material, the shock impedance, Z_i is easily substituted here as

$$Z_i = \rho_0 u_s = \rho_0 (C_0 + s(v_f - u_p)). \tag{9}$$

We used two different windows to reach two shock states in the liquid flyer, as shown in Figure 7b, giving two shock impedances for a single v_f and ρ_0. Subtracting the shock impedances from one another gives ρ_0,

$$\rho_0 = \frac{Z_2 - Z_1}{s(u_{p1} - u_{p2})}. \tag{10}$$

Thus, if the slope of the linear Hugoniot is known, the initial density can be calculated from shock states reached by a single flyer velocity into two different impedance materials. Substituting Equation 10 into Equation 8 yields,

$$P = \frac{Z_2 - Z_1}{s(u_{p1} - u_{p2})} (C_0 + s(v_f - u_p))(v_f - u_p). \tag{11}$$

The only unknowns in this equation are s and C_0. We fit Equation 11 to the two window shock states and the initial ~0 pressure state of the flyer using a least squares regression, determining the values of s and C_0. We then used these fitted parameters to calculate the initial density using Equation 10.

Experiments on the same Z target panel with the same measured impact velocity, within error, were averaged together, propagating uncertainty as uncorrelated, random error. The fitted Hugoniot for the liquid flyer is well constrained using Equation 11. An example experiment is shown in Figure 8. Small residuals are present in the fitted liquid Hugoniot, as in Figure 8, demonstrating the limits of the assumed linear Hugoniot. The limited number of data points prevents fitting to higher orders without risking an under

Table 5
Averaged Results for Each Z Experiment

Shot #	Sam. u_s (km/s)	P (GPa)	S (kJ/K/kg)	Liq. v_f (km/s)	Qtz u_s (km/s)	TPX u_s (km/s)	s (–)	C_0 (km/s)	ρ_{0L} (kg/m^3)	Shock T (K)	Release T (K)
Z2792	14.56 ± 0.21	325.45 ± 2.98	4.68 ± 0.46	15.47 ± 0.19	13.62 ± 0.05	15.87 ± 0.07	1.21 ± 0.43	3.98 ± 1.25	2,274 ± 294	9,232 ± 530	4,078 ± 1,084
Z2868	15.42 ± 0.10	368.45 ± 1.87	4.97 ± 0.45	16.43 ± 0.22	14.05 ± 0.05	16.49 ± 0.10	1.16 ± 0.48	4.19 ± 1.42	2,184 ± 318	11,098 ± 425	4,716 ± 1,299
Z2879° N	13.46 ± 0.30	263.97 ± 3.57	4.28 ± 0.48	12.93 ± 0.25	12.03 ± 0.02	13.98 ± 0.05	1.13 ± 0.33	4.37 ± 1.08	2,422 ± 268	7,160 ± 600	3,387 ± 874
Z2879 S	13.97 ± 0.15	293.89 ± 2.11	4.48 ± 0.46	14.07 ± 0.14	12.76 ± 0.07	14.81 ± 0.03	1.24 ± 0.389	3.91 ± 1.09	2,313 ± 239	8,080 ± 405	3,674 ± 942
Z3422	16.32 ± 0.10	428.53 ± 2.05	5.24 ± 0.46	17.87 ± 0.16	14.56 ± 0.04	17.38 ± 0.05	0.97 ± 0.26	5.16 ± 1.06	2,102 ± 177	13,268 ± 501	5,484 ± 1,496

Notes. Covariance matrices for s and C0 are given in the supporting information. Shock temperatures for forsterite (T) were calculated from the T(us) relation in Table 2 from Root et al. (2018). The release temperatures are predicted temperatures as discussed in Section 3.2. N and S denote the north and south panel of the same shot as each panel was impacted by an aluminum flyer with a different velocity. Other shots were either performed with symmetric velocities or forsterite samples were only on one panel.

constrained problem. However, all residuals are within the 1σ uncertainty of the liquid Hugoniot. The calculated initial density, and fitted parameters s and C_0 are given in Table 5, along with the averaged data. The liquid densities calculated here, along with apparent temperatures from Table 4, are presented with their corresponding shock states in Figure 9.

3.2. Optical Depth and Temperature of the Decompressing Sample

To better understand the physical context of the apparent temperature measurement, it is important to compare the measurement to predictions of the temperature along an isentrope and to examine the optical path in more detail. This section presents a prediction of the liquid-vapor phase boundary temperature using data from Root et al. (2018) and Davies et al. (2020) and then a calculation of how the apparent temperatures of liquid layer are depressed from the true material temperature due to droplets in the optical path, following the methods from Kraus et al. (2012).

Temperature on an isentrope can be calculated using the Grüneisen parameter, γ, as

$$\gamma = -\left(\frac{d\ln T}{d\ln V}\right)_S. \tag{12}$$

Under the Mie-Grüneisen approximation, the temperature along an isentrope can be calculated through a finite difference. Approximating infinitesimal steps along the isentrope and substituting specific volume with density, starting from a known temperature and density, temperature on the isentrope is given by

$$T_k = \exp\Big(\gamma(\rho_k)[\ln\rho_k - \ln\rho_{k-1}] + \ln T_{k-1}\Big), \tag{13}$$

where subscript k are the steps on the isentrope. The $\gamma(\rho)$ relationship for forsterite is taken from Davies et al. (2020) and presented in Table 2. Starting from the shock state of experiments in Table 5, temperature is calculated over the decompression path until the liquid density is reached. For densities below 2,597 kg/m^3, the 1 bar density of liquid forsterite (Thomas & Asimow, 2013), the γ relation is not valid. Below this density, γ is held constant at the 2,597 kg/m^3 value. Holding γ constant effectively makes this prediction an estimate. The predicted liquid temperature for shot Z3422, the highest pressure reverse impact experiment, is hotter than all of the apparent temperatures measured in Section 2.2, despite the measured apparent temperatures being associated to stronger shocks.

To explain the cooler apparent temperatures than predicted, the optical depth of the liquid-vapor mixture in front of the liquid flyer in the optical path must be considered. To calculate the optical depth, the density profile of the decompressing mixture must be calculated.

At a given time, the density profile in Eulerian coordinates can be calculated from the characteristics in Figure 5 by considering conservation of mass:

$$\int_{x_0}^{x(\rho_i)} dx = \int_0^{h(\rho_i)} \frac{\rho_0}{\rho} dh, \tag{14}$$

where x_0 is a constant of integration that depends on momentum transfer through the release path (Kraus et al., 2012). Density profiles, shown in Figure 5a, were calculated for the example 430 GPa shock experiment at 5, 10, and 15 ns after breakout at the free surface. The profiles were calculated up to the peak shock density, and the x_0 offset is calculated by the sound speed of the highest density characteristic to obtain an estimation of the distance propagated by the rarefaction wave up range into the sample.

With the density gradient in front of the density plateau that defines the liquid layer, the optical depth can be calculated in a similar manner as in Kraus et al. (2012) and Lock et al. (2018). The average absorption, α, for an infinitesimal slice in the liquid-vapor mixture is given as

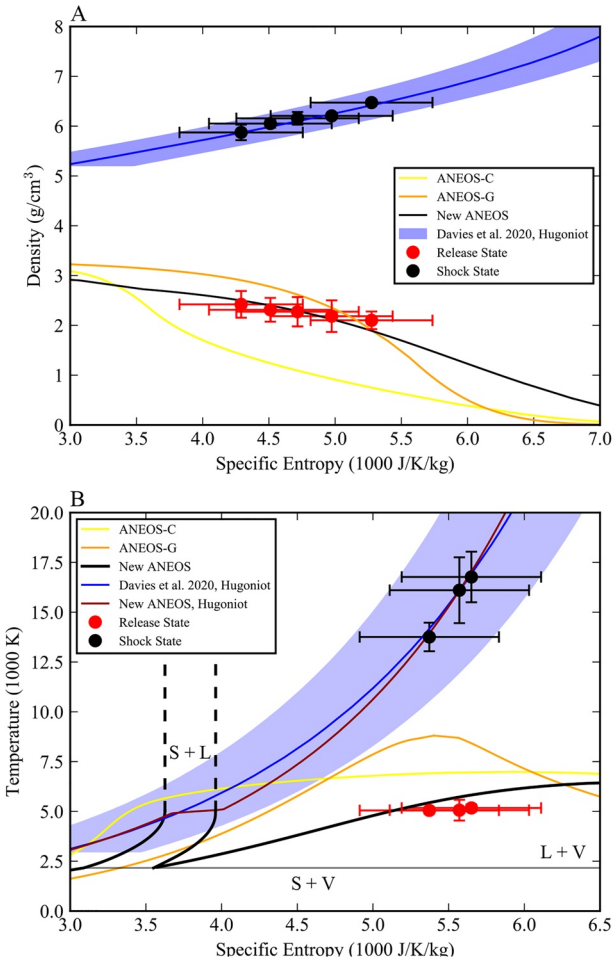

Figure 9. (a) Experimentally determined density and specific entropy of states on the liquid-vapor curve (red points) and their associated shock states (black points). (b) Measured apparent temperatures and specific entropies of states on the liquid-vapor curve and their associated shock states. The blue curve, with 1-σ error envelope, is the experimentally determined forsterite principal Hugoniot (Davies et al., 2020; Root et al., 2018). The yellow (ANEOS-C, Canup et al., 2013) and orange (ANEOS-G, Ćuk & Stewart, 2012; Nakajima & Stevenson, 2014) lines are different forsterite ANEOS models previously used in giant impact simulations. The ANEOS model for forsterite was recently revised by Stewart et al. (2020) (new ANEOS); the new ANEOS model phase boundaries are shown by black lines and the model Hugoniot in brown lines. The gray line denotes the triple point temperature. The shock states (black points) decompress along an isentrope to intersect the vapor curve (red points).

$$\alpha(x)dx = \frac{dx}{L_{\mathrm{mfp}}(x)} + \alpha_{\mathrm{vap}}(x)dx, \tag{15}$$

where L_{mfp} is the photon mean free path distance in a cloud of spherical liquid condensates, and α_{vap} is the absorption coefficient of the vapor phase. This expression assumes that the liquid is perfectly absorbing. Previous work on silica showed that the liquid condensate term is dominant (Kraus et al., 2012), and we assumed that α_{vap} for forsterite can be neglected for the length scale of the experiment.

The mean free path of a photon through a cloud of spherical condensates is given as

$$L_{\mathrm{mfp}} = \frac{4}{6D}\frac{\rho_{\mathrm{liq}}}{\rho_{\mathrm{bulk}}}, \tag{16}$$

where D is the condensate diameter, ρ_{liq} is the liquid density on the phase boundary, and ρ_{bulk} is the isentrope bulk density of the liquid-vapor mixture. Each position in Figure 10a is associated to a state on the isentrope, and densities below the density plateau also have an associated liquid density on the liquid-vapor phase boundary. We considered a range of droplet sizes (100–1,000 nm) based on other types of shock-vaporization experiments at the laboratory scale (Sedoi et al., 1998; Tkachenko et al., 2004) because the range of condensate diameters during our experiments is not known.

The average photon from an emitting layer is likely to interact with a silicate droplet where the optical depth is equal to or greater than one,

$$\int_{x_{fs}}^{x(L=1)} \alpha(x)dx \geq 1, \tag{17}$$

where x_{fs} is the Eulerian position of the decompressing free surface, ~150 μm in the 430 GPa case at 10 ns, and x ($L = 1$) is the depth of the emitting layer at an optical depth of one. At Eulerian positions farther from the free surface than x ($L = 1$), the emitted photons of the hotter, higher density layers are likely to be absorbed, and the measured emission spectrum reflects a cooler, lower density layer. Thermal emission from cooler, less dense layers are neglected. Figure 10b shows the forsterite model liquid-vapor dome from (Stewart et al., 2020) and predicted apparent release temperatures at 10 ns after breakout. Depending on condensate size, there is a large range of possible apparent temperatures, which overlaps our experimentally measured apparent temperatures. Given the neglected vapor absorption term in this work, the measured apparent temperatures in Table 4 do not serve as a robust constraint on the absorbing condensate droplet diameter. However, this calculation shows that the optical depth of the absorbing condensate droplets down range of the liquid layer affects the measured apparent temperature. Furthermore, experiments at lower specific entropies are less affected by the presence of the liquid-vapor mixture leading the liquid layer.

3.3. Experiment and Measurement Uncertainty

Uncertainties for reverse impact experiments (Table 3) stem from a number of sources. Shock velocity and liquid flyer velocity calculated from time of flight measurements depend on uncertainties in the thickness

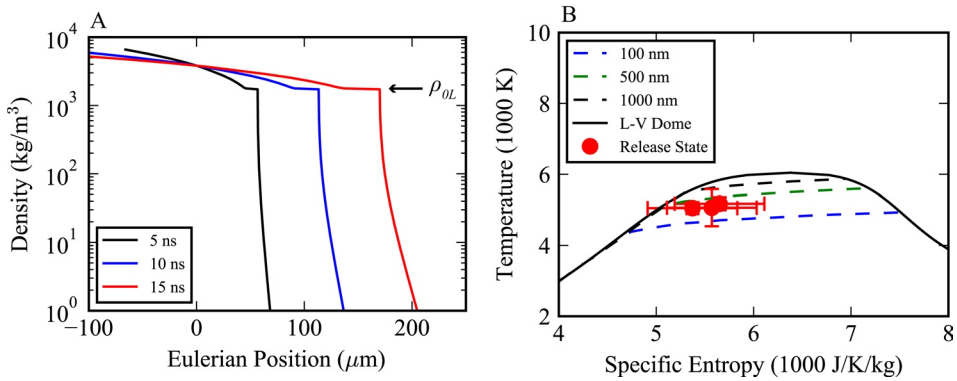

Figure 10. (a) Density profiles in Eulerian coordinates at different times after release from a downrange free surface in an experiment with shock pressure of 430 GPa. The liquid density plateau is denoted by ρ_{0L}. (b) Liquid-vapor phase boundary in $T-S$ space, where the dashed lines are the predicted observed apparent temperatures due to absorption of droplets ahead of the liquid layer. Larger liquid condensates in the liquid-vapor mixture causes the optical depth to become shorter, obscuring the temperature emission from the liquid wall.

of the samples or gap, as well as uncertainties in the VISAR diagnostic itself. For VISAR measurements of reflecting shock velocities in standard windows, uncertainty is independent of sample thickness.

Experiments with impact velocities within their measured uncertainties, typically on the same shot panel, are averaged together to reduce uncertainty. Uncertainty of each measurement is propagated and combined with the standard deviation for each parameter. Shock states of forsterite, α-quartz, and TPX (pressure, density, entropy, and temperature) are calculated from the measured shock velocity and the relations in Table 2. Uncertainty for these calculations and the density measurement are propagated through a *Monte Carlo* uncertainty analysis technique. All variables with measured uncertainty are randomly perturbed according to a normal distribution about their $1-\sigma$ uncertainty. The calculations are repeated with such random perturbations until the resulting data cloud converges to a Gaussian, typically after 10,000 steps. The mean of the Gaussian is taken as the fitted value, and the standard deviation to be the $1-\sigma$ uncertainty.

The apparent temperature measurement uncertainty is found in a similar way to the density. Parameters are perturbed and the temperature emission is continuously re-fit until the resulting data cloud converges. An additional 2% uncertainty is added to all temperature measurements to account for the ideal greybody assumption of the quartz standard and possible non-linearity of the SVS response function as described in Root et al. (2018). Shot Z3033 has elevated uncertainty compared to the experiments on shot Z3172 due to light contamination of the of the time window for the experiment. During the final stage of an experiment, expanding material from the experiment impact the probe, creating an intense flash that is recorded in the science frame. Light from this event may bleed or overexpose the science frame. The current experimental setup accounts for this effect by increasing the distance from the free surface of the down range sample to the probe and gating the probe impact in time. Post-shock emission from shot Z3033 is contaminated by probe impact light and a single ideal blackbody does not fit the emission spectrum. However, smaller sections of the emission spectrum are well fit by a blackbody. For shot Z3033, three sub sections of the emission spectrum are fit independent of the others. Wavelengths 440–520 nm are fit by 5,514 ± 351 K, 520–580 nm by 5,142 ± 312 K, and 580–640 nm by 4,534 ± 178 K. These sections are then averaged together, propagating the calculated uncertainties and the standard deviation to receive the result shown in Table 4.

3.4. EOS Model Development

Figure 9 shows the measured shock and release data compared to different ANEOS-based models for forsterite. Older material models used in previous works on planetary collisions, ANEOS-C (Canup et al., 2013) and ANEOS-G (Ćuk & Stewart, 2012; Nakajima & Stevenson, 2014), were developed before high-pressure data were available for forsterite. Pressure-density-temperature (Root et al., 2018) and entropy (Davies et al., 2020) data on the forsterite principal Hugoniot showed that these parameter sets over predicted

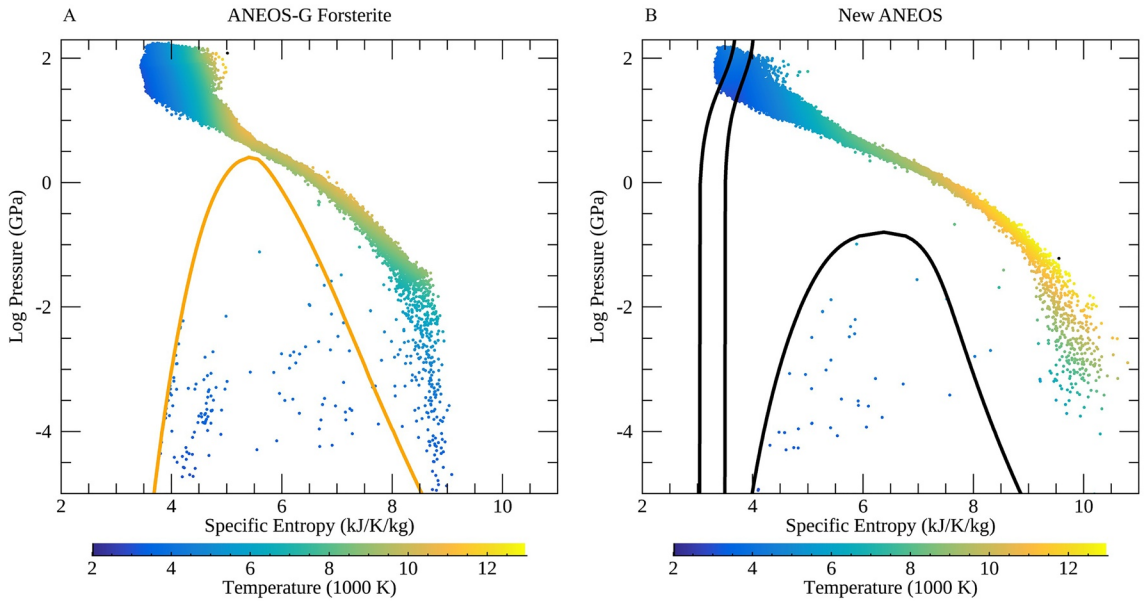

Figure 11. Thermal profiles through the Earth after a canonical Moon-forming impact event, comparing two forsterite EOS models for the mantle: ANEOS-G (a) and New ANEOS (b). Dots show the pressure-entropy in the midplane (±1,000 km) within the Roche radius compared to the phase boundaries (orange line: vapor curve from ANEOS-G; black lines are the melt curve and vapor curve from New ANEOS. The highest pressures are at the core-mantle boundary and the lowest pressures are in the disk. The pressure profiles through the mantle and disk fall above the forsterite critical point. ANEOS, Analytic Equations of State; EOS, equations of state.

temperature and under predicted specific entropy. Furthermore, the liquid-vapor dome states measured here do not agree with the model liquid-vapor dome of either of these older forsterite ANEOS models.

The high pressure measurements on the principal Hugoniot (Davies et al., 2020; Root et al., 2018), preliminary analyses of the experiments presented in this work, and constraints on the critical point, now published in Townsend et al. (2020), were used to constrain a revised forsterite ANEOS-based model (labeled New ANEOS). The ANEOS code package was updated to include a user adjustable heat capacity in the liquid and was focused on fitting high pressure Hugoniot data and the liquid and vapor regions of the phase diagram, see Stewart et al. (2020). This forsterite ANEOS model (version SLVTv1.0G1, Stewart et al., 2019) provides a good fit to the shock Hugoniot, liquid-vapor curve, and isentropes connecting the Hugoniot and vapor curve up to several 100s GPa. This model's critical point also agrees well with ab initio calculations of the forsterite critical point (Townsend et al., 2020) at $\rho_c = 0.52 \pm 0.03$ g/cm^3, $T_c = 6{,}240 \pm 200$ K, and $P_c = 0.13 \pm 0.02$ GPa.

3.5. Improved Thermodynamics of Giant Impacts

Past models of the forsterite principal Hugoniot, ANEOS-C and ANEOS-G, underestimate the production of entropy from a shock front (Davies et al., 2020). The forsterite ANEOS (version SLVTv1.0G1) is a better fit to the shock temperatures and entropies generated in the giant impact regime. Furthermore, the liquid-vapor dome has much better agreement with our experimental constraints compared to previous models. Giant impact simulations that rely on this new EOS will have decompression paths that involve more vaporization compared to past models with the same impact parameters. To illustrate the effects of the reformulated EOS, we present the temperature-specific entropy profiles through the Earth after a canonical Moon-forming giant impact (e.g., Canup, 2004), where a Mars-mass body obliquely strikes the proto-Earth near the mutual escape velocity. The giant impact calculations are described in Appendix C of Supporting Information. Two post impact cases of the canonical moon forming giant impact (Canup et al., 2013) are shown. In Figure 11, we compare the thermal states in the mantle with two different EOS models for forsterite (ANEOS-G and New ANEOS). In both examples, the proto-Earth mass was 0.9 M_{Earth}, the impactor was 0.13 M_{Earth}, and the impact velocity was 9.2 km/s. In the ANEOS-G case, the impact parameter was 0.74,

and in the new ANEOS case, the impact parameter was 0.7. The simulations used the GADGET-2 smoothed particle hydrodynamics code with 206,000 particles. Each point represents a mantle particle in the mid-plane at 48 h after the impact.

The enhanced production of entropy on the shock Hugoniot from New ANEOS, a phenomena described in detail in Davies et al. (2020), leads to generally higher entropy in the entire post impact mantle. In the ANEOS-G model, the critical point was at much higher pressures, densities, and temperatures than we expect from current constraints. In simulations using this model, the thermal profile through the Earth after the giant impact fell just above the critical point (as pointed out in [Lock & Stewart, 2017]). Note that the ANEOS-G model did not include a melt curve. Using the New ANEOS forsterite model, the specific entropies are larger compared to the previous model and the critical point is lower. Using criteria for supercritical conditions defined here as $T > T_{\text{critical}}$ and $P > P_{\text{critical}}$, the mass fraction of the mantle that reaches supercritical conditions is 0.123 using ANEOS-G and 0.188 using New ANEOS. As a result, the case that much of the Earth's mantle reaches the supercritical fluid regime during the Moon-forming giant impact is much more robust with our new experimentally constrained EOS model.

4. Conclusions

This study presents the results from multiple experiments on forsterite that map the thermodynamic path of the shock-and-release process. We presented the results from two types of experiments on the Sandia Z Machine: Shock-and-release experiments to measure the post-shock emission spectrum and reverse impact experiments that constrain the density of the liquid branch of the liquid-vapor phase boundary.

Forsterite is widely used in numerical simulations of planetary collisions as an analog material for the mantles of terrestrial planets. The constraints to the forsterite phase diagram provided here directly augment and improve the effort to understand the formation of terrestrial planets.

Using the data here and in previous studies of forsterite, a new EOS model for forsterite has been formulated to more accurately track the evolution of the thermodynamics of collision events. The thermodynamic structure of a planet after a giant impact is sensitive to the material EOS model. For the extreme shock pressures reached in giant impacts, past models have underestimated the entropy of the forsterite principal Hugoniot. Previously, the liquid-vapor phase boundary was not constrained, and the constraints provided from this work improve the predictions from giant impact simulations. Future studies of impact simulations should implement the experimentally constrained model.

Real mantles of Earth-like planets probably never consist of pure forsterite. However, olivine with about 90% forsterite and 10% fayalite (Fe_2SiO_4) makes up about 60% of the Earth's upper mantle, while the rest is enstatite ($MgSiO_3$), diopside ($CaMgSi_2O_6$), and pyrope ($Mg_3Al_2Si_3O_{12}$), all with an Fe-content similar to that in olivine. Future experiments should explore the effects that inclusion of these additional components have on the calculated thermodynamic paths in planetary collisions. The experiments and analyses presented here serve as a model for investigating the effects of the additional components that must be present in any Earth-like planetary mantle.

Data Availability Statement

The revised ANEOS parameter set for forsterite, modifications to the ANEOS code, and SESAME and GADGET format EOS tables are available at https://github.com/isale-code/M-ANEOS and Stewart et al. (2019). All scripts used for calculations, supporting spreadsheets, and additional figures in this work are available at Davies et al. (2021).

Acknowledgments
This work was conducted under the Z Fundamental Science Program. The authors thank the support from DOE-NNSA grant DE-NA0003842 and DE-NA0003904, NASA grants NNX-15AH54G and NNX16AP35H, and UC Office of the President grant LFR-17-449059. Sandia National Laboratories is a multimission laboratory managed and operated by National Technology and Engineering Solutions of Sandia, LLC., a wholly owned subsidiary of Honeywell International, Inc., for the U.S. Department of Energy's National Nuclear Security Administration under contract DE-NA0003525. This paper describes objective technical results and analysis. Any subjective views or opinions that might be expressed in the paper do not necessarily represent the views of the U.S. Department of Energy or the United States Government. This work was performed under the auspices of the U.S. Department of Energy by Lawrence Livermore National Laboratory under Contract DE-AC52-07NA27344. The authors would like to express thanks to the reviewers for their helpful comments.

References

Asimow, P. D. (2018). Melts under extreme conditions from shock experiments. In *Magmas under pressure* (pp. 387–418). Elsevier.
Barker, L. M., & Hollenbach, R. E. (1972). Laser interferometer for measuring high velocities of any reflecting surface. *Journal of Applied Physics*, *43*(11), 4669–4675. https://doi.org/10.1063/1.1660986
Barker, L. M., & Schuler, K. W. (1974). Correction to the velocity-per-fringe relationship for the VISAR interferometer. *Journal of Applied Physics*, *45*(8), 3692–3693. https://doi.org/10.1063/1.1663841

Canup, R. M. (2004). Simulations of a late lunar-forming impact. *Icarus*, *168*(2), 433–456. https://doi.org/10.1016/j.icarus.2003.09.028
Canup, R. M., Barr, A. C., & Crawford, D. A. (2013). Lunar-forming impacts: High-resolution SPH and AMR-CTH simulations. *Icarus*, *222*(1), 200–219. https://doi.org/10.1016/j.icarus.2012.10.011
Celliers, P., Loubeyre, P., Eggert, J., Brygoo, S., McWilliams, R., Hicks, D., & Collins, G. (2010). Insulator-to-conducting transition in dense fluid helium. *Physical Review Letters*, *104*(18), 184503. https://doi.org/10.1103/physrevlett.104.184503
Chambers, J. (2010). *Terrestrial planet formation*. University of Arizona Press. (297–317).
Costa, G. C. C., Jacobson, N. S., & Fegley, B., Jr. (2017). Vapourization and thermodynamics of forsterite-rich olivine and some implications for silicate atmospheres of hot rocky exoplanets. *Icarus*, *289*, 42–55. https://doi.org/10.1016/j.icarus.2017.02.006
Cuk, M., & Stewart, S. T. (2012). Making the Moon from a fast-spinning Earth: A giant impact followed by resonant despinning. *Science*, *338*(6110), 1047–1052. https://doi.org/10.1126/science.1225542
Davies, E., Duncan, M., Root, S., Kraus, R., Spaulding, D., Jacobsen, S., & Stewart, S. (2021). edavi006/forsterite_stagnation: Temperature and density on the forsterite liquid-vapour phase boundary (version v1.01). *Zenodo*. https://doi.org/10.5281/zenodo.3981597
Davies, E. J., Carter, P. J., Root, S., Kraus, R. G., Spaulding, D. K., Stewart, S. T., & Jacobsen, S. (2020). Silicate melting and vapourization during rocky planet formation. *Journal of Geophysical Research: Planets*, *125*, e2019JE006227. https://doi.org/10.1029/2019JE006227
Deer, W., Howie, R., & Zussman, J. (2013). An introduction to the rock-forming minerals. In *Mineralogical society of Great Britain and Ireland, London* (p. 498).
Hicks, D., Boehly, T., Eggert, J., Miller, J., Celliers, P., & Collins, G. (2006). Dissociation of liquid silica at high pressures and temperatures. *Physical Review Letters*, *97*(2), 025502. https://doi.org/10.1103/physrevlett.97.025502
Knudson, M., & Desjarlais, M. (2009). Shock compression of quartz to 1.6 TPa: Redefining a pressure standard. *Physical Review Letters*, *103*(22), 225501. https://doi.org/10.1103/physrevlett.103.225501
Knudson, M., & Desjarlais, M. (2013). Adiabatic release measurements in α-quartz between 300 and 1200 GPa: Characterization of α-quartz as a shock standard in the multimegabar regime. *Physical Review B*, *88*(18), 184107. https://doi.org/10.1103/physrevb.88.184107
Kraus, R. G., Root, S., Lemke, R. W., Stewart, S. T., Jacobsen, S. B., & Mattsson, T. R. (2015). Impact vapourization of planetesimal cores in the late stages of planet formation. *Nature Geoscience*, *8*(4), 269. https://doi.org/10.1038/ngeo2369
Kraus, R. G., Stewart, S. T., Swift, D. C., Bolme, C. A., Smith, R. F., Hamel, S., et al. (2012). Shock vapourization of silica and the thermodynamics of planetary impact events. *Journal of Geophysical Research*, *117*(E9). https://doi.org/10.1029/2012je004082
Lemke, R., Knudson, M., Bliss, D., Cochrane, K., Davis, J.-P., Giunta, A., & Slutz, S. (2005). Magnetically accelerated, ultrahigh velocity flyer plates for shock wave experiments. *Journal of Applied Physics*, *98*(7), 073530. https://doi.org/10.1063/1.2084316
Lock, S. J., & Stewart, S. T. (2017). The structure of terrestrial bodies: Impact heating, corotation limits, and synestias. *Journal of Geophysical Research Planets*, *122*(5), 950–982. https://doi.org/10.1002/2016je005239
Lock, S. J., Stewart, S. T., Petaev, M. I., Leinhardt, Z. M., Mace, M. T., Jacobsen, S. B., & Ćuk, M. (2018). The origin of the Moon within a terrestrial synestia. *Journal of Geophysical Research: Planets*, *123*(4), 910–951. https://doi.org/10.1002/2017JE005333
Melosh, H. J. (2007). A hydrocode equation of state for SiO2. *Meteoritics & Planetary Sciences*, *42*(12), 2079–2098. https://doi.org/10.1111/j.1945-5100.2007.tb01009.x
Millot, M., Dubrovinskaia, N., Cernok, A., Blaha, S., Dubrovinsky, L., Braun, D. G., et al. (2015). Shock compression of stishovite and melting of silica at planetary interior conditions. *Science*, *347*(6220), 418–420. https://doi.org/10.1126/science.1261507
Nagahara, H., Kushiro, I., & Mysen, B. O. (1994). Evapouration of olivine: Low pressure phase relations of the olivine system and its implication for the origin of chondritic components in the solar nebula. *Geochimica et Cosmochimica Acta*, *58*(8), 1951–1963. https://doi.org/10.1016/0016-7037(94)90426-x
Nakajima, M., & Stevenson, D. J. (2014). Investigation of the initial state of the Moon-forming disk: Bridging SPH simulations and hydrostatic models. *Icarus*, *233*, 259–267. https://doi.org/10.1016/j.icarus.2014.01.008
Rice, M., McQueen, R. G., & Walsh, J. (1958). Compression of solids by strong shock waves. *Solid State Physics*, *6*, 1–63.
Root, S., Mattsson, T. R., Cochrane, K., Lemke, R. W., & Knudson, M. D. (2015). Shock compression response of poly (4-methyl-1-pentene) plastic to 985 GPa. *Journal of Applied Physics*, *118*(20), 205901. https://doi.org/10.1063/1.4936168
Root, S., Townsend, J. P., Davies, E. J., Lemke, R. W., Bliss, D. E., Fratanduono, D. E., & Jacobsen, S. B. (2018). The principal Hugoniot of forsterite to 950 GPa. *Geophysical Research Letters*, *45*(9), 3865–3872. https://doi.org/10.1029/2017GL076931
Sedoi, V., Valevich, V., & Chemezova, L. (1998). Production of submicron aerosols by the exploding wire method. *Journal of Aerosols*, *4e*, 41–47.
Stewart, S., Davies, E., Duncan, M., Lock, S., Root, S., Townsend, J., & Jacobsen, S. (2019). Equation of State Model Forsterite-ANEOS-SLVTv1.0G1: Documentation and Comparisons (Version v1.0.0). *Zenodo*. https://doi.org/10.5281/zenodo.3478631
Stewart, S., Davies, E., Duncan, M., Lock, S., Root, S., Townsend, J., & Jacobsen, S. (2020). The shock physics of giant impacts: Key requirements for the equations of state. In *21st Biennial APS conference on shock compression of condensed matter (SCCM19)*. AIP Publishing. in press (arXiv:1910.04687v2).
Stewart, S. T., & Ahrens, T. J. (2005). Shock properties of H_2O ice. *Journal of Geophysical Research*, *110*(E3). https://doi.org/10.1029/2004je002305
Thomas, C. W., & Asimow, P. D. (2013). Direct shock compression experiments on premolten forsterite and progress toward a consistent high-pressure equation of state for CaO-MgO-Al2 O3 -SiO2 -FeO liquids. *Journal of Geophysical Research: Solid Earth*, *118*(11), 5738–5752. https://doi.org/10.1002/jgrb.50374
Thompson, S. L. (1990). *ANEOS analytic equations of state for shock physics codes input manual*. (Technical Report). Sandia National Labs. https://doi.org/10.2172/6939284
Thompson, S. L., & Lauson, H. S. (1974). *Improvements in the Chart D radiation-hydrodynamic CODE III: Revised analytic equations of state*. (Technical Report Nos. SC-RR–71-0714). Sandia Labs.
Tkachenko, S. I., Vorob'ev, V. S., & Malyshenko, S. P. (2004). The nucleation mechanism of wire explosion. *Journal of Physics D Applied Physics*, *37*(3), 495. https://doi.org/10.1088/0022-3727/37/3/030
Townsend, J. P., Shohet, G., & Cochrane, K. R. (2020). Liquid-vapour coexistence and critical point of Mg 2 SiO 4 from ab initio simulations. *Geophysical Research Letters*, *47*(17), e2020GL089599. https://doi.org/10.1029/2020gl089599
Zel'Dovich, Y. B., & Raizer, Y. P. (2002). *Physics of shock waves and high-temperature hydrodynamic phenomena*. Courier Corporation.

References From the Supporting Information

Carter, P. J., Lock, S. J., & Stewart, S. T. (2020). The energy budgets of giant impacts. *Journal of Geophysical Research Planets*, *125*(1), e2019JE006042. https://doi.org/10.1029/2019JE006042

Fiquet, G., Auzende, A. L., Siebert, J., Corgne, A., Bureau, H., Ozawa, H., & Garbarino, G. (2010). Melting of Peridotite to 140 Gigapascals. *Science*, *329*(5998), 1516–1518. https://doi.org/10.1126/science.1192448

Marcus, R. A. (2011). *The role of giant impacts in planet formation and internal structure*. (Ph.D. thesis). Harvard University.

McGlaun, J. M., Thompson, S., & Elrick, M. (1990). Cth: A three-dimensional shock wave physics code. *International Journal of Impact Engineering*, *10*(1–4), 351–360. https://doi.org/10.1016/0734-743x(90)90071-3

Springel, V. (2005). The cosmological simulation code GADGET-2. *Monthly Notices of the Royal Astronomical Society*, *364*(4), 1105–1134. https://doi.org/10.1111/j.1365-2966.2005.09655.x

Stewart, S. T. (2020). Equation of State Model Fe85Si15-ANEOS: Development and documentation (Version SLVTv0.2G1). *Zenodo*. https://doi.org/10.5281/zenodo.3866550